

Long-term-average, solar cycle, and seasonal response of magnetospheric energetic electrons to the solar wind speed

D. Vassiliadis,¹ A. J. Klimas,² S. G. Kanekal,³ D. N. Baker,³ and R. S. Weigel⁴

Received 28 September 2001; revised 15 November 2001; accepted 20 November 2001; published 19 November 2002.

[1] Among the interplanetary activity parameters the solar wind speed is the one best correlated with the energetic electron fluxes in the inner magnetosphere. We examine the radial and temporal characteristics of the 2–6 MeV electron response, approximating it in this paper with linear filters. The filter response is parameterized by the time delay (τ), measured from the time of solar wind impact, and the L shell (L). We examine solar cycle and seasonal effects using an 8-year-long database of Solar, Anomalous, and Magnetospheric Particle Explorer (SAMPEX)/ Proton Electron Telescope (PET) measurements at the radial range $L = 1.1$ – 10 . The main peak P_1 of the long-term-average response is at $(\tau, L) = (2, 5.3)$ and has a simultaneous response over a wide range of radial distances, $\Delta L = 5$. The duration of the response after the peak is inversely proportional to the L shell. The central part of the inner magnetosphere ($L = 3.7$ – 5.75) has a much more prolonged response (>10 days) than other parts. Prior to the main response, P_1 , a brief response, P_0 , of typically lower amplitude appears at $(\tau, L) = (0, 3)$, probably as a quasi-adiabatic response to the compression of the magnetosphere by the solar wind pressure. Over the solar cycle the variation in solar wind input results in a systematic change of the position, amplitude, radial extent, and duration of the two peaks: during solar wind minimum the quasi-adiabatic peak disappears, and the radial size of the responding region decreases; both are responses to low-density, high-speed streams. During solar minimum, the duration is at least 3 days (30%) longer than average, probably due to the sustained solar wind input. Systematic variations appear also as a function of season due to several magnetic and fluid effects. During equinoxes the coupling is stronger, and the duration is longer (by at least 2 days) compared to solstices. Between the two equinoxes the fall response has a significantly higher amplitude and longer duration than the spring equinox response. This is at least partly due to the higher GSE B_y component during the observation time, which acts to increase the effective GSM B_z component according to the Russell-McPherron effect. The seasonal modulation of the response is consistent with the variation in the fluxes themselves [Baker *et al.*, 1999]. The modulation is discussed in terms of the equinoctial and axial hypotheses [Boller and Stolov, 1970; Russell and McPherron, 1973; Cliver *et al.*, 2000].

INDEX TERMS: 2730 Magnetospheric Physics: Magnetosphere—inner; 2720 Magnetospheric Physics: Energetic particles, trapped; 2784 Magnetospheric Physics: Solar wind/magnetosphere interactions; 2788 Magnetospheric Physics: Storms and substorms; 2740 Magnetospheric Physics: Magnetospheric configuration and dynamics; **KEYWORDS:** radiation belts, inner magnetosphere, solar cycle, seasonal variability, relativistic electrons, magnetic storms

Citation: Vassiliadis, D., A. J. Klimas, S. G. Kanekal, D. N. Baker, and R. S. Weigel, Long-term-average, solar cycle, and seasonal response of magnetospheric energetic electrons to the solar wind speed, *J. Geophys. Res.*, 107(A11), 1383, doi:10.1029/2001JA000506, 2002.

¹Universities Space Research Association, NASA Goddard Space Flight Center, Greenbelt, Maryland, USA.

²NASA Goddard Space Flight Center, Greenbelt, Maryland, USA.

³Laboratory for Atmospheric and Space Physics, University of Colorado, Boulder, Colorado, USA.

⁴National Research Council, NASA Goddard Space Flight Center, Greenbelt, Maryland, USA.

1. Introduction

[2] The mechanism of energetic particle production in Earth's radiation belts constitutes a largely unresolved problem [Li and Temerin, 2001] albeit with broad significance for astrophysical and planetary physics. In the last decade interest in this issue has been steadily increasing because of the recognition of detrimental effects produced on spacecraft by energetic particles [e.g., Koons *et al.*,

1999]. It is important to distinguish regular and climatological variations of the radiation flux from individual responses, since they establish the baselines from which fluctuations and large-scale disturbances can be defined and modeled. In this paper we present a series of models for the long-term and regular variations.

[3] The electron radiation belts are extremely dynamic regions, continually replenished by acceleration and transport of particles. These processes most probably take place within the magnetosphere since the interplanetary medium is not a sufficient source or acceleration region for these populations [Baker *et al.*, 1989; Li *et al.*, 1997]. The exact acceleration mechanisms are unknown, but observations support the following framework. Relativistic electron fluxes j have been linked to increases in solar wind speed V_{SW} , notably during high-speed streams [Paulikas and Blake, 1979]. The correlation between j and V_{SW} is moderate (at a level of 40–60%), but higher than that between the fluxes and any other interplanetary variable, including the interplanetary magnetic field (IMF). This implies that the energy transfer involves at least one mechanism different from magnetic reconnection which is determined mainly by the Southward part of the IMF B_z component. For example the solar wind flow past the magnetospheric obstacle excites fluid instabilities (Kelvin-Helmholtz, etc.) at the boundary. These are important in transferring momentum and energy to the magnetosphere, especially so at its low-latitude flanks [Farrugia *et al.*, 2001]. The instabilities generate ultra-low-frequency (ULF) waves in the range Pc4-5 which propagate radially as well as azimuthally and couple large regions of the inner magnetosphere. ULF wave amplitudes also correlate well with electron flux levels with a 1-day delay [Rostoker *et al.*, 1998]. Simulations show that the lower modes of ULF-wave electric field can resonantly accelerate test particles, representing the seed electrons, to high energies [Elkington *et al.*, 1999]. Alternatively, pitch angle scattering of the electrons off high-frequency waves leads to diffusion in energy within realistic timescales of several hours [Liu *et al.*, 1999]. A very probable source for the low-energy, or “seed,” electrons of energies of 10–100 keV is the substorm activity that takes place simultaneously at high latitudes. This framework is consistent with the correlations between solar wind speed and electron fluxes, and ULF wave amplitudes and electron fluxes. Recently, the significance of the solar wind speed input has been demonstrated by an empirical diffusion model which is driven mainly by V_{SW} time series and is capable of reproducing the electron fluxes at the geosynchronous region at a relatively high accuracy [Li *et al.*, 2001].

[4] In this paper we use a linear approximation of the response of the electron flux in the inner magnetosphere to the solar wind speed. Clearly the effective physical coupling is nonlinear, e.g., linear changes in velocity result in exponential changes in particle flux [Paulikas and Blake, 1979]. However, given the significance of the solar wind speed [Li *et al.*, 2001], a linear approximation is a reasonable first step and provides a baseline in modeling the response. To that end we have chosen linear filters. These can represent the temporal features of the prolonged, time-delayed response [e.g., Baker *et al.*, 1990]. In addition, linear filters lend themselves to physical interpretation more

easily than higher-order approximations. Finally, the linear filter responses are numerically robust so we can compare responses for different times and radial distances. This allows us to take full advantage of the spatial and temporal coverage (in L shell as well as season and solar cycle phase) provided by the SAMPEX data set. Higher-order approximations, such as nonlinear filters and neural networks, can be developed as extensions of linear filters in subsequent work. These are known to be more accurate than linear methods for describing flux dynamics [e.g., Koons and Gorney, 1991], although typically less amenable to physical interpretation.

[5] The paper is structured as follows: the electron flux and solar wind measurements are described in the next section. Section 3 presents the lagged correlation between the fluxes and solar wind and the next section introduces the linear filters. Sections 5, 6, and 7 present the results on the long-term-average response, the solar cycle variation and the seasonal variation, respectively.

2. Electron Flux and Solar Wind Plasma Measurements

[6] The relativistic electron fluxes we use have been recorded by the Proton Electron Telescope (PET) [Cook *et al.*, 1993] on board the Solar, Anomalous, and Magnetospheric Particle Explorer (SAMPEX). The spacecraft was launched in 1992 and is in a low-altitude (600-km), high-inclination (82°) orbit with a period of approximately 1.5 hours. The PET instrument provides omnidirectional flux measurements of >0.4 MeV electrons. We use daily-averaged measurements from the ELO channel, which was designed to measure 2–6 MeV. The fluxes are mapped to nominal L shell distances using the IGRF model. The measurements include both precipitating and trapped flux; these cannot be distinguished because the detector has a rather large acceptance angle and its pointing direction is not known.

[7] To compare the electron flux levels to solar wind speed variations we have used interplanetary data from the OMNI database of the National Space Science Data Center (NSSDC) at a daily resolution. The database has been put together from measurements from several spacecraft. These are at different geocentric distances, but the solar wind propagation time from their position to Earth is usually an hour or less, so it is negligible when compared to the daily resolution.

2.1. SAMPEX/PET Measurement Uncertainties

[8] The SAMPEX orbit and the PET detector design [Cook *et al.*, 1993] impose certain limitations in the measurement quality in two regions. First, the flux of MeV-energy electrons is significantly reduced at high L shells: in the range of $L = 7–10$ the counts are a few tens of particles per L shell bin per orbit. The design and operation of the PET instrument as a coincidence detector result in a much smaller number of recorded counts at those distances than in the lower L shells. Even under those conditions, it should be noted that some of the statistical results in sections 3 and 5–7 are smoothly continuous across these L shell ranges so it is reasonable that these correlations are representative of physical effects.

[9] Second, in the near-Earth region, and in particular during the traversal of the slot and inner zone ($1.1 < L < 3$), the ELO measurements may be contaminated by protons (members of the SAMPEX team, private communication, 2001). Therefore the results presented in sections 3 and 5–7 for those particular L shells should be interpreted in terms of a more general particle flux response rather than one that involves only energetic electrons.

[10] An additional factor of uncertainty, especially for large L shell values (>6), is the magnetic field model. The data used in this study have been mapped using the IGRF model, but even the more realistic approximations are not free of ambiguity (e.g., see cautionary remarks by *Selesnick and Blake* [2000]). In summary for most results the focus is in the range $L = 3–7$. However, we also note the smooth continuation of the results at distances $L > 7$.

2.2. Statistical Distribution of the Electron Flux

[11] For modeling purposes one can choose between the original fluxes J and some other function, for instance the logarithmic flux (log-flux), $j \equiv \log_{10} J$. While physically the change of variable may not be significant, there are practical reasons that lead to a preference of the log-flux [e.g., *Nagai*, 1988; *Baker et al.*, 1990; *Tsutai et al.*, 1999; *Li et al.*, 2001]. The probability density function of the flux, $P(J)$, is extremely asymmetric with respect to the average, and all probability moments are ill-defined. High-flux measurements ($>10^4$ particles /sr cm² sec) are essentially outliers and skew the parameter estimation results. Therefore the flux data cannot be used effectively for estimation of model parameters. In contrast to that, the probability distribution of the logarithmic flux j at a given L shell is much closer to Gaussian (normal) so models derived from it have a reasonable fitting error. This is evident from examining the distribution at a range of L shells ($L = 4–8$). In the remainder of the paper we will mostly use the logarithmic flux j and on occasion we will repeat the analysis for the flux J .

3. Correlation Between Solar Wind Speed and Energetic Particle Fluxes

[12] It is known that there is a delay of 2–3 days between the solar wind speed changes at the magnetopause and the corresponding change in energetic electron flux at geosynchronous orbit [*Baker et al.*, 1990]. This timescale is determined by the slowest process(es) in the chain of events that produce electron acceleration and transport.

[13] To identify both the time and radial location of highest correlation in j with the solar wind speed V_{SW} we use the correlation function

$$C_{V_{SW}, j_e}(\tau; L) = \frac{1}{T} \frac{1}{\sigma_{V_{SW}} \sigma_{j_e}} \sum_{t=1}^T (V_{SW}(t) - \langle V_{SW} \rangle)(j_e(t + \tau; L) - \langle j_e(L) \rangle). \quad (1)$$

[14] The correlation (1) is shown as a function of time delay τ and L shell in Figure 1a. The time delay is measured from the time of solar wind impact on the magnetopause. For the long-term-average response the summation time T represents the entire database (1993–2000). Therefore the correlation retains only the linear relation between the two

variables and will average over any nonlinear, seasonal, and other individual features.

[15] We note several characteristics of the correlation (1) evident in Figure 1a:

1. Simultaneous correlation for many L shells: For a wide range of radial distances ($L = 4.0–9.3$) the highest value of the correlation, $C_{V_{SW}, j_e}^{(\max)}(\tau^{(\max)}; L)$, occurs at $\tau^{(\max)}(L) = 2–3$ days independently of L. This is consistent with the response timescale of 2 days found by *Baker et al.* [1990] for fluxes at the geosynchronous orbit. This delay time encompasses the growth time of ULF waves as well as the time delay of 1 day between electron flux increases and ULF waves found by *Rostoker et al.* [1998]. Note that the correlation does not distinguish between radial transport and local acceleration because only one energy channel is examined.

2. Peak correlation: The highest value of the correlation occurs at $L = 7.4$ with a width of about 0.5 L. The peak value is moderate (approximately 35%) so equation (1) does not account for a large percentage of the variance in j . The rest should be attributed to nonlinear processes and/or additional solar wind input parameters.

3. Peak variability with L shell: Although the onset of the response is approximately simultaneous (within one day or less) for a wide range of L shells, the peak and duration of the correlation occur earlier at large distances than closer to Earth. For that radial range the maximum at a given L shell occurs approximately at time

$$\tau_{C\max}(L) = -0.277L + 3.77, \quad 3.9 \leq L \leq 9.3. \quad (2)$$

For $L = 6.6$ we obtain $\tau = 1.94$ which is close to the second-day peak found by *Baker et al.* [1990].

4. Longest duration: The correlation at $L \sim 4$ lasts more than 10 days. This is much longer than the passage time of large transient solar wind structures such as magnetic clouds. This duration represents the time of magnetospheric memory to solar wind input rather than the autocorrelation of the solar wind speed (which is less than 5 days [*Baker et al.*, 1990]).

5. Response in the slot and inner zone: There is a low correlation between the solar wind speed and fluxes in those regions. The slot is in the range 2–2.5 typically while the inner zone is earthward of the slot, between 1.5 and 2. The slot region has a lower correlation than most L shells of the outer zone ($L > 3$) because electrons pitch-angle scatter and are rapidly lost in that region. Interestingly, the inner zone has a higher correlation than the slot, and sometimes that correlation is comparable to that of the outer zone. Note, however, that, as mentioned in section 2.1, fluxes measured at $L < 3$ may represent a more general particle response including contamination by low-energy ions.

[16] We also examine the correlation between V_{SW} and the original (not logarithmic) fluxes J . The correlation function is in some respects similar to that for j (Figure 1b). As before the interpretation of the main peak is that there is a delay of >1 day relative to the solar wind, consistent with the results of linear prediction filtering for geosynchronous-orbit data [*Baker et al.*, 1990]. Again, this is the time necessary for either development of ULF waves and inward transport or local acceleration of electrons by the waves.

[17] However, there are also differences between the two. Both the duration and radial size of the correlation are lower for $C_{V_{SW}, J}$ than for $C_{V_{SW}, j}$. Here the peak correlation is at $L =$

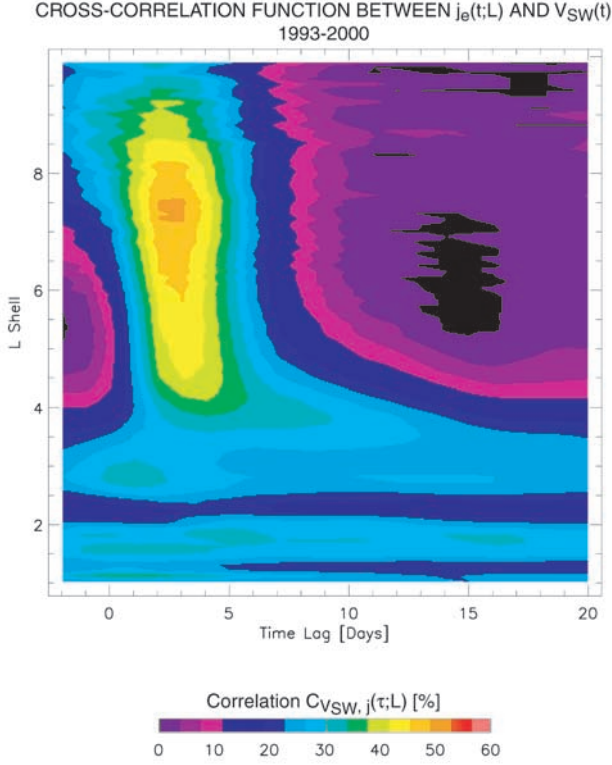


Figure 1a. The lagged cross-correlation function $C_{V_{SW}, j}$, equation (1), between solar wind speed V_{SW} and the electron log-flux j at a fixed L shell is shown as a function of time lag τ and L shell. This is the average correlation, computed from 8 years of data (1993–2000). The high-correlation region is indicative of the radiation belt source region.

4.6 instead of $L = 7.4$. Also the size of the spatial region of highest correlation with V_{SW} is reduced. We measure it as the range of L where the correlation exceeds a given threshold value, C_{min} . For example, for $C_{min} = 0.35$ the ranges for the two correlations are

$$\begin{aligned} C_{j_e, V_{SW}}(L) &\geq 0.35 : 4.0 \leq L \leq 9.3 \\ C_{J_e, V_{SW}}(L) &\geq 0.35 : 3.8 \leq L \leq 5.4 \end{aligned} \quad (3)$$

so the log-flux is correlated with the solar wind speed over a region which more than three times as large. This is because the log-flux j_e gives a much greater weight to the low fluxes compared to J_e . Equation (3) shows that V_{SW} correlates with the low-amplitude fluctuations over a wide range of L shells whereas it correlates with the high-amplitude fluxes only within a small radial range. Note that there is a temporal aspect to this, as well: the linear correlation with the log-fluxes j is high over a wide region at an early stage (when the fluxes are still low) rather than at the end of the acceleration period (by which time the fluxes J have developed nonlinearly).

4. Temporal and Spatial Scales of the Coupling: Linear Filtering

[18] While the correlation provides some information about time and space scales of the coupling, it is not useful

in distinguishing between changes due to the magnetospheric response and simultaneous changes in the solar wind input. One way to reduce this ambiguity is to approximate the dynamic response of the flux levels by using linear moving-average (MA) filters (sometimes called “linear prediction filters”) [Clauer, 1986]. We consider that the flux $j(\tau; L)$ at a given L shell at time lag τ is determined to a significant extent by the magnetospheric response to previous solar wind speed variations going back in time up to $\tau - T$. The timescale T represents the effective memory to V_{SW} of the processes determining the electron flux levels. The actual energy expended during particle acceleration is made available through many processes in the solar wind-magnetosphere interaction whose net effect is represented by a response function. We write the electron flux as a response to V_{SW} variations and consider only the linear part:

$$j_e(t; L) = \int_{-T_S}^T H(\tau; L) V_{SW}(t - \tau) d\tau + \dots \quad (4)$$

The ellipsis denotes higher-order (nonlinear) terms and the effect of lesser solar wind parameters that are not taken into account here. Equation (4) weighs the effectiveness of each prior input $V_{SW}(t - \tau)$ by a factor $H(\tau; L)$ for a particular L shell. In the linear approximation the impulse response

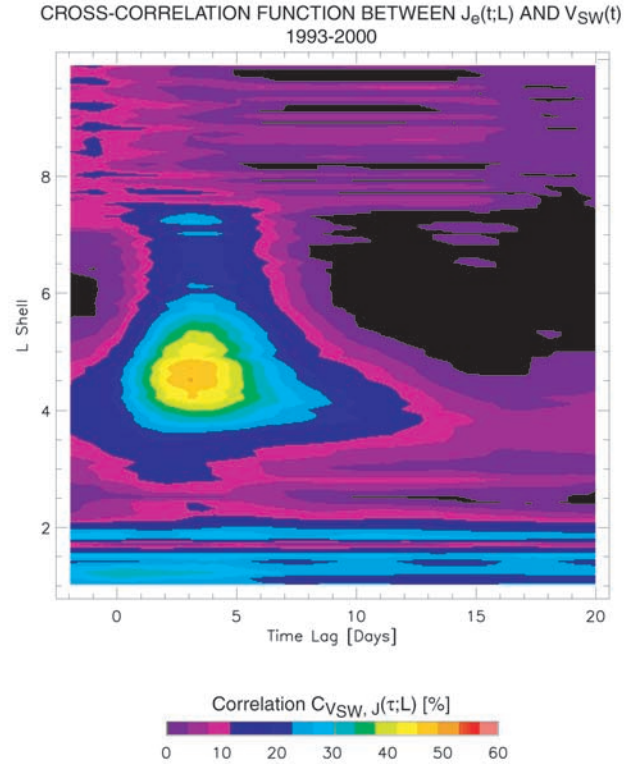


Figure 1b. Similar plot for the correlation function $C_{V_{SW}, J}$ using the flux J rather than the log-flux j . This correlation peaks at a lower radial distance than $C_{V_{SW}, j}$ because J emphasizes high fluxes which usually occur deep in the magnetosphere.

function H is independent of the observation interval (and therefore of the activity level) so the effects of successive inputs to the flux at a fixed L shell are simply additive.

[19] Equation (4) is solved for $H(\tau; L)$ whose peaks specify temporal scales and, since it is parameterized by L , also spatial scales. We use a matrix inversion technique based on singular value decomposition [Press *et al.*, 1993]. The technique also provides confidence limits (estimated variances) $\delta H(\tau; L)$ for the coefficients $H(\tau; L)$ based on the variance of the input and output data. The impulse response function defines a model for the fluxes at shell L :

$$\hat{j}(t; L) \equiv \int_{-T_s}^T H(\tau; L) V_{SW}(t - \tau) d\tau. \quad (5)$$

[20] As mentioned, the duration T represents the effective memory of the processes determining the electron flux to previous inputs. Since it is a free parameter, we choose $T = 21$ days so that it is clearly below the 27-day solar wind recurrence time. Filters with $T = 11$ give qualitatively similar results, but poorer fitting (lower correlation between model and data as defined below). Filters with $T = 6$ have significantly lower correlations between filter output and observed fluxes than those with $T = 21$. The starting time T_s is nominally zero, but for numerical stability it is set to a finite value ($T_s = 5$).

[21] For clarity we repeat the assumptions made in the linear approximation of the electron response as equation (4):

1. Among the possible interplanetary inputs we examine only the effect of V_{SW} . The solar wind speed is the variable that correlates best with log-fluxes [Paulikas and Blake, 1979]. For example, the magnetic field B_z component is significant at timescales of substorms and even for storms, but not as significant as the several-day-long acceleration processes that we are interested in here. Therefore we do not examine it below. Following the Paulikas and Blake [1979] study many subsequent reports have either neglected the B_z effect [Nagai, 1988; Baker *et al.*, 1990] or considered it less important than V_{SW} [Li *et al.*, 2001]. Solar wind density and temperature as well as the B_y component are even less well correlated with particle fluxes than V_{SW} and B_z . The effects of these other parameters will be addressed in a future study.

2. Time-stationarity: The physical processes that accelerate electrons vary at many different timescales. The approach (4) is valid for processes that change slowly compared to the duration T . As we will see in sections 6 and 7 there are systematic changes with season and phase of the solar cycle, that is, for timescales much longer than T .

3. Linearity: While the j response to interplanetary parameters is most probably nonlinear, a linear approximation is useful in providing an upper bound on the significance of the linear component in (4). We expect that nonlinear models will account for much of the remaining variance (e.g., as discussed by Koons and Gorney [1991]). Here we quantify the accuracy of the fit as well as the linearity of the response by using the correlation between filter output $\hat{j}(t; L)$ and observed fluxes $j(t; L)$:

$$C_{j,j}(L) = \frac{1}{T\sigma_j\sigma_j} \sum_{t=1}^T \left(\hat{j}(t; L) - \langle \hat{j}(L) \rangle \right) \left(j(t; L) - \langle j(L) \rangle \right) \quad (6)$$

The percentage of the variance in the data that equation (5) is able to reproduce is approximately the square of the correlation (6).

4. Since the response is defined for each L shell separately it does not explicitly represent radial diffusion or convection: However, some of these transport effects can be inferred by examining responses from many neighboring L shells.

5. The Long-Term-Average Linear Response

[22] We first obtain the long-term-average linear response for a given L shell by fitting equation (4) to the 8-year-long time series of the flux. Such a fitting averages out any nonlinear and non-stationary effects in the response. Any peculiarities, in terms of V_{SW} , of individual solar wind structures are also averaged out. The only remaining effect in V_{SW} may be a weak variation with the solar cycle; to that end we discuss solar cycle effects below.

[23] The linear filters $H_4(t)$ and $H_{6.6}(t)$ for $L = 4$ and 6.6 , respectively, give temporal information for the onset, amplitude, and end of the linear response in these regions (Figure 2a). The largest contribution to the flux at both L shells is made at peak P_1 , which appears at lag

$$\tau_{P_1} \cong 2 \text{ days}$$

following a change in the solar wind. The peak of the response $H_{6.6}(t)$ measured by SAMPEX is similar to the one found from geosynchronous spacecraft data [Baker *et al.*, 1990]. Note that the peak amplitude at the geosynchronous orbit is stronger than for $L = 4$. On the other hand the duration of the part of the response function following the peak is $T - \tau_{P_1} > 9 \text{ days}$ for $L = 4$ compared to $T - \tau_{P_1} > 5 \text{ days}$ at the geosynchronous orbit. In fact, after day 6 the response at $L = 6.6$ becomes negative so changes in V_{SW} that are older than 6 days are weakly anticorrelated with the fluxes. The negative response means that the effects of the fluctuations in V_{SW} are more effective in scattering the electrons than accelerating them. On average then, the coupling to solar wind speed is more sustained, and therefore effectively stronger, in the earthward part of the outer radiation belt than at geosynchronous orbit.

[24] The uncertainties $\delta H(\tau; L)$ in the filter coefficients $H(\tau; L)$, as calculated by the solution of equation (4), are shown by the small (almost invisible) vertical error bars in Figure 2a. The error bar size is so small, $|\delta H(\tau; L)/H(\tau; L)| \leq 2 \times 10^{-3}$, because the size of the data set used in the fitting reduces the statistical uncertainty in the coefficients.

[25] The model-data correlation (6) is 41.3% and 41.6% for $L = 4$ and $L = 6.6$, respectively. The amount of variance in the data explained by the filters is roughly the square of this correlation, or 16%. Therefore the filters can only be interpreted as qualitative indicators of the response. However, we expect that nonlinear filters will represent a greater part of the response, as has been shown for fluxes at the geosynchronous orbit [Koons and Gorney, 1991].

[26] The response also varies systematically as a function of radial distance. Figure 2b shows the response (4) as a two-parameter function $H(\tau; L)$. Several features are discerned:

1. Peak response: The peak response, P_1 , occurs at $L_{H \max} = 5.4$. As already seen in the correlation plot of Figure 2a, the largest contribution to electron fluxes at any L shell occurs 1–3 days after the onset of the change in V_{SW} . This

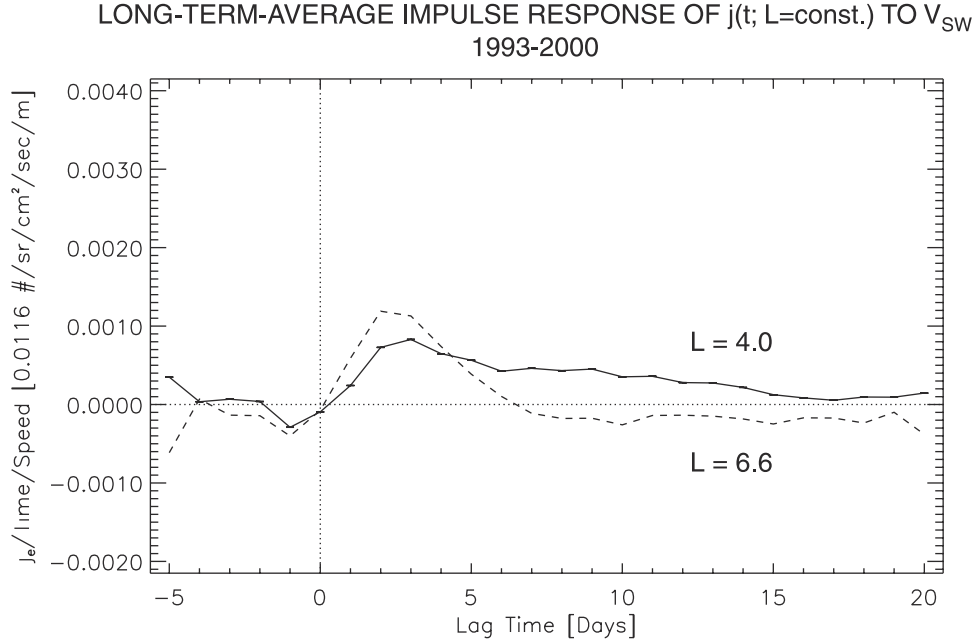


Figure 2a. Impulse response functions $H_L(\tau)$ from equation (4) for $L = 4$ (solid line) and $L = 6.6$ (dashed line). These are the linear approximations of the long-term response at those L shells, computed from 8 years of data (1993–2000). The peak responses are approximately equal, but the response at the heart of the inner zone lasts about 10 days more than the one at geosynchronous orbit.

response may be related to the source region, i.e. the region where most of the nonadiabatic acceleration occurs (see definition of the source region by *Selesnick and Blake* [2000]). Here we examine fluxes rather than phase space density, so strictly speaking we do not distinguish adiabatic from nonadiabatic effects. The filters in Figure 2, however, are calculated from a very larger number of intervals with different conditions, so some adiabatic effects such as the response to the ring current or pressure pulses are averaged out. Therefore the response in Figure 2b and in particular the peak P_1 may be related to nonadiabatic effects.

2. Simultaneous response over a wide range of radial distances: During the peak response (on day 2) a wide range of L shells responds approximately simultaneously. The near-simultaneous flux enhancement at all L shells is consistent with the coherent response seen concurrently in many regions of the inner magnetosphere [*Kanekal et al.*, 1999]. The largest range, measured as the range where $H(\tau; L) \geq H_{\min} = 5 \times 10^{-3}$, is $\Delta L = 5$.

3. Scaling of the response duration: For L shells in the range $L = 3.7$ – 8.6 the duration of the response after day 2 drops rapidly. For a given threshold H_{\min} , the region where $H \geq H_{\min}$ has a well-defined duration. The duration as a function of L can be fit with a double-linear decay:

$$T(L) = \begin{cases} a_1(L - 3.7) + b_1, & \tau_{P_1} < \tau \leq \tau_b \\ a_2(L - 3.7) + b_2, & \tau_b \leq \tau \end{cases} \quad (7)$$

The breakpoint τ_b is found by maximizing the correlation between the data and the fit. For a range of H_{\min} the slopes and intercepts of the two lines and the breakpoint are shown in Table 1. The fitted lines are shown in a contour plot in Figure 2c. The approximate breakpoint location is marked with a vertical dotted line.

Right after the peak P_1 the response duration is approximately inversely proportional to T . After day 7, however, the response at most L shells is negligible except for $L = 3.7$ – 5.75 where it decreases much more slowly. The slope a_2 of $T(L)$ is small, between $1/6$ and $1/10$ of the steeper slope a_1 . Note the similarity of the timescales in (7) with the timescale of the correlation in equation (2). The maximum duration of (7) occurs at $L = 4.1$ and is $T_{\max} \cong 12$ days.

These timescales for the late response are determined by convection, diffusion, and loss of the particles accelerated up until $\tau = 2$ days. Here the reader is reminded that the impulse response represents the electron flux time profile after an idealized solar wind speed input in the form of an impulse, $V_{SW}(t) \sim \delta(t)$. Thus the response after the P_1 peak is the flux that model (5) would predict in the absence of any subsequent solar wind inputs and geomagnetic activity. Under quiet geomagnetic conditions the decay of the radiation belts is mainly due to pitch angle scattering of the electrons into the atmosphere [*Abel and Thorne*, 1998]. For comparison, measurements of the decay of the phase space density of 3–8 MeV electrons towards a quiescent state show a much steeper dependence of the lifetime with L shell [*Selesnick et al.*, 1997]. This comparison is limited, however, since here we are using the flux rather than the phase space density and do not explicitly remove adiabatic effects as *Selesnick et al.* [1997] have done.

4. Quasi-adiabatic response: A minor peak, P_0 , occurs at $(\tau; L) = (0; 3.25)$. As the solar wind speed increases, the enhanced ram pressure ρV_{SW}^2 causes a magnetospheric compression and trapped particles move to lower altitudes. This effect appears here as an increase of fluxes at lower L shells. After the pressure pulse has subsided, the electrons drift back to higher altitudes and the fluxes at near-Earth

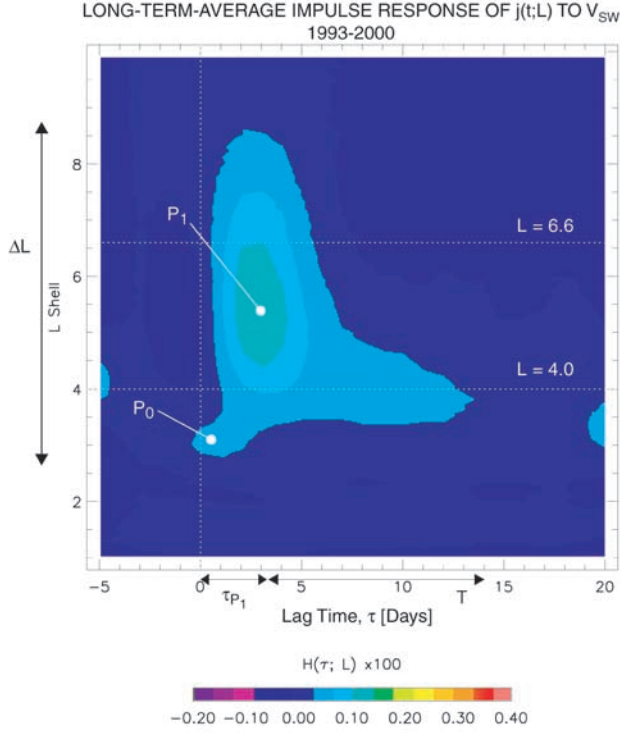


Figure 2b. Impulse response functions for all L shells in the range 1–10 for the same data as in Figure 4a shown here as a two-dimensional response function versus time delay τ and L shell. This spatiotemporal response is characterized by a radial size ΔL and duration T . High-amplitude regions such as P_1 are probably representative of the location and time of the acceleration and/or transport for the 2–6 MeV electrons. The P_1 peak is related to the 2-day long acceleration process following an enhancement in the solar wind speed. Note the similarity of this peak with the peak of Figure 1. A second high-response region, peak P_0 , is a transient, quasi-adiabatic response to the compression associated with an increase in the solar wind speed. The individual responses have been smoothed in the τ direction with a running average of 2 days. No smoothing has been performed in the L direction. The L shells of 4 and 6.6 are marked with dotted lines.

distances rapidly decrease. This transient effect is a quasi-adiabatic response to the interplanetary pressure variation. However, the process is irreversible because the third adiabatic invariant is violated (the timescale of the interaction is sufficiently long for this to occur), and inward radial

diffusive transport and trapping takes place. Electrons that are transported below $L \sim 3$ enter the slot region and are lost. Therefore the peak is adjacent to that region. (We use the term “quasi-adiabatic” because with a single energy channel and with a rather simple magnetic field model we cannot separate adiabatic from non-adiabatic effects. However, the occurrence of this response at $\tau = 0$ and its very brief duration suggest that part of it is an adiabatic effect.)

This response is probably related to the sudden appearance of energetic electrons deep in the magnetosphere, at $L = 3$ –4, observed at the beginning of a CME passage [Baker *et al.*, 1998]. It is significantly different that the slower buildup of the radiation belt populations under sustained high-speed driving. It is possible that under unusually strong compressions this effect may be observed at even lower L shells. Rapid compression and non-adiabatic effects can culminate in the formation of transient belts at L as low as 2–2.5 (e.g., during the passage of an interplanetary shock as shown by Li *et al.* [1993], where the electric field acceleration violated the third adiabatic invariant). After the P_0 response has decayed within 2–3 days, the response in the region $L = 3$ –3.5 is much lower than that of region $L = 4$ –6.

5. Flux decrease prior to the main solar wind impact: On day $\tau = -1$ the response has a shallow minimum, V_1 , clearly seen in Figures 2a and 2c and less so in Figure 2b. The minimum at negative τ is robust for all reasonable choices of filter parameters and preprocessing, and does not seem to be a numerical effect. The same decrease has been observed in the response of geosynchronous-orbit fluxes to either the solar wind or even geomagnetic indices (in the latter case the minimum is more brief) [Baker *et al.*, 1990].

[27] These are the main features of the linear response. Some of them bear direct analogies to features of the correlation in Figure 2a. It should be noted that while we have used a linear technique (equation (4)) to approximate the flux response, the results show the significant non-linearity of the processes: the correlation (6) for the most interesting region, $L = 3$ –8, is in the range 30–50%. This nonlinearity will be explored with linear and nonlinear filters in a future study.

[28] Some similarities exist between the linear response of j and that of J (Figure 3). The peak response occurs at $L = 4.3$. Here, however, the duration is much smaller. Also there is no comparable response in the region $L > 6.6$.

[29] The correlations (6) as a function of L shell are shown for the logarithmic and the regular fluxes in Figure 4. For reference, the L shells of 4.0 and 6.6 are denoted with vertical dotted lines. High correlation values identify regions where the linear filter is accurate in representing the speed-flux coupling; the correlation of $C = 0.70$ (where

Table 1. Radial Transport Rates Derived From the Response $H(\tau; L)^a$

H Contour, d^{-1}	$T(L) = a_1(L - 3.7) + b_1$		Breakpoint τ_b , days	$T(L) = a_2(L - 3.7) + b_2$		Correlation, %
	a_1 , days	b_1 , days		a_2 , days	b_2 , days	
0.00005	−0.10595	2.4541	8	−1.2219	7.9031	97.21
0.00010	−0.16528	2.7133	7	−1.2415	7.7405	98.39
0.00020	−0.15851	2.2107	9	−0.9977	6.2591	98.01
0.00030	−0.16399	1.9181	7	−1.0905	6.0649	97.28
0.00050	−0.09999	1.5000	6	−1.1551	5.3686	91.55
0.00075	−0.10000	1.7000	5	−1.1000	4.5000	85.57

^a Radial transport rates are given as slopes a_i of the double linear fit (7) of the response $H(J;L)$ in Figure 2c. The breakpoints τ_b and the correlation coefficient of the fit are also given.

LONG-TERM-AVERAGE IMPULSE RESPONSE OF $j(t;L)$ TO V_{sw}
1993-2000

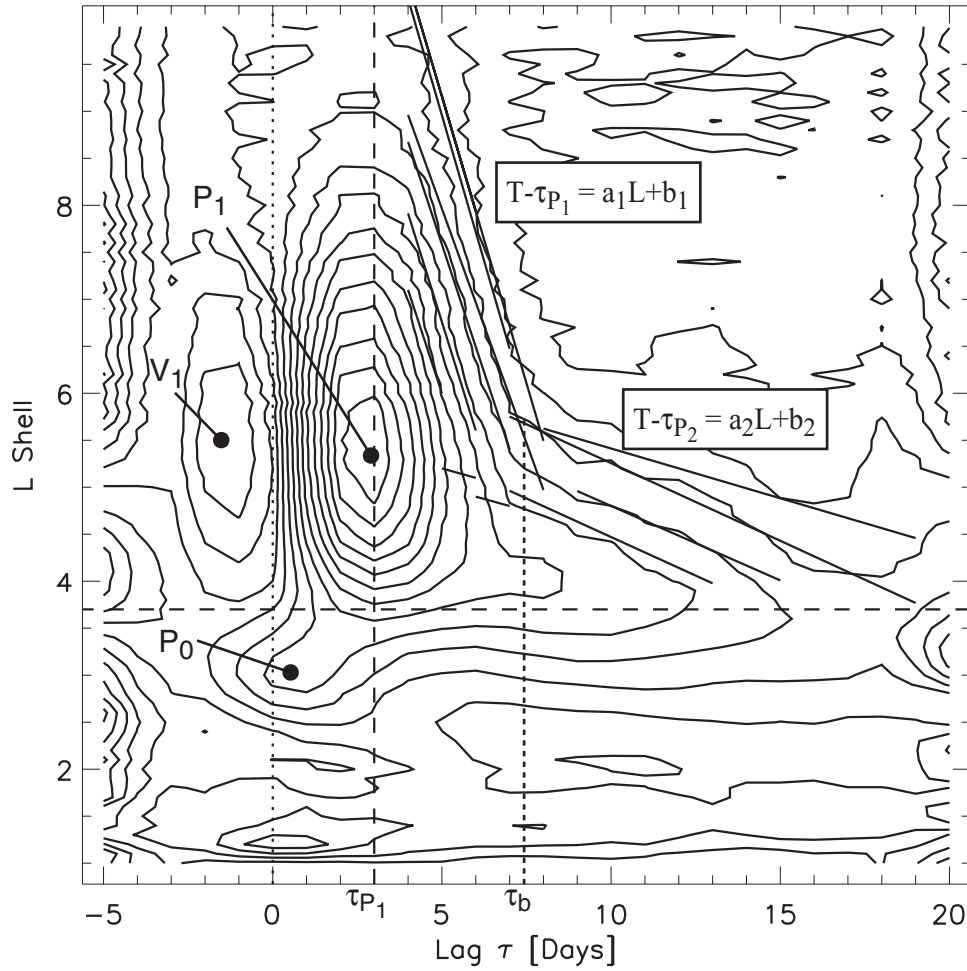


Figure 2c. Same as Figure 2b; in addition the minimum V_1 is denoted indicating a precursor signal, of particular interest in improving predictability of the disturbance. For reference, the time lag of $\tau = 3$ days is marked with a vertical dotted line and the L shell of 3.7 is marked with a horizontal dashed line. Here we focus our attention on the late response (>3 days), which has two well-separated stages and; thereby, implications for radial transport and acceleration. The first stage is the rapid decay of the P_1 peak while the second stage, starting at $\tau_b = 7.5$ days, is a prolonged acceleration and/or trapping at L shells below 6.0. The duration of the coupling for a given H contour is approximated with a double linear fit (pairs of straight lines) as shown in Table 1. A vertical dotted line at $\tau = 7.5$ days denotes the approximate position of the breakpoint.

49% of the variance is reproduced) is denoted by a horizontal dotted line. The region of high correlation is wider for the log-fluxes rather than the regular fluxes. For example the region where is $C_{j,j}(L) > 0.35$ is $\Delta L \cong 5$ whereas the corresponding region for J is only $\Delta L \cong 1.5$ wide. Note also that the correlation for the log-fluxes is weakly bimodal, peaking at approximately 3.7 and 6.0. These two peaks correspond to P_0 and P_1 , respectively, as will be more clearly evident in the solar cycle and seasonal variations.

6. Effect of Solar Cycle Phase

[30] The variation of the solar wind over the solar cycle provides a systematic way to examine how the electron flux responds to different types of input sequences. In

terms of geoeffective structures, maxima are characterized by a predominance of coronal mass ejections, with high density and moderately high velocity, while minima and the descending part of the cycle often contain high-speed streams with relatively lower average density [Crooker, 2000]. Occurrence of interplanetary shocks increases with the sunspot number and other measures of solar activity [Volkmer and Neubauer, 1985].

[31] We calculate the response for four 2-year-long data sets with the solar minimum being represented by 1995–1996 and the maximum by 1999–2000. We note the following features pertaining to the solar cycle (SC):

SC1. Overall similarity to the long-term-average response: We examine impulse responses H_4 and $H_{6.6}$ for the corresponding key regions (Figure 5a). In all cases H_4 is

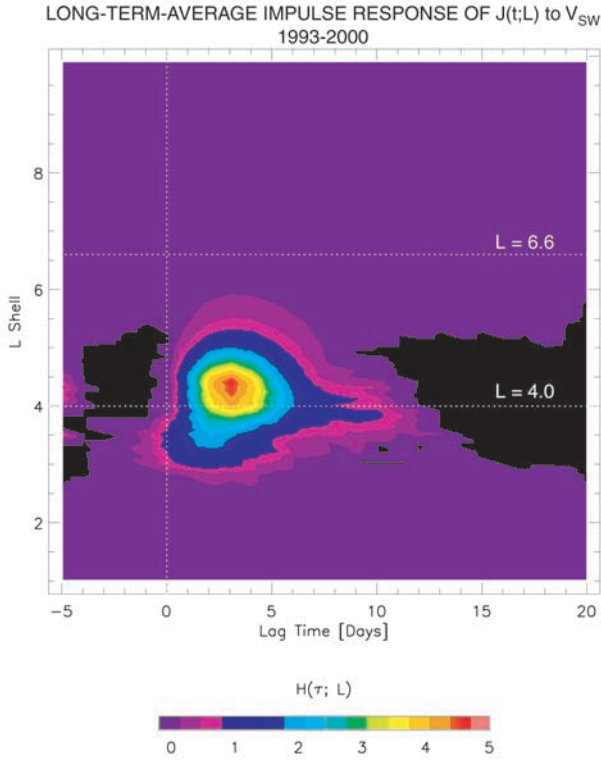


Figure 3. Same as in Figure 2b, but for the fluxes J rather than the log-fluxes j .

longer-lived than $H_{6.6}$, but the geosynchronous response is usually larger in peak amplitude and occurs somewhat earlier. Both responses display the shallow minimum V_1 before the zero lag. These three properties are in agreement with the long-term-average response (Figure 2a) and are evidence of its robustness under different driving conditions.

SC2. Variation with solar cycle phase: Between the responses at the two L shells, the geosynchronous one shows the largest change: the peak amplitude increases by a factor of 2 during 1995–1996 and 1997–1998 than in the other years or the long-term average. Also the peak rises earlier in 1997–1998 and becomes sharper at solar minimum. In terms of duration the geosynchronous response increases by 3 days at solar minimum (1995–1996). Similar changes occur for the H_4 response whose duration increases even more for the same years and for 1997–1998. The changes for $L = 4$ and 6.6 are characteristic for the responses at many L shells between 3 and 9 (Figure 5b):

SC3. Maximum duration at solar minimum: The response becomes longer by >10 days during solar minimum than in any other epoch. This sustained response is probably the effect of streams whose velocity is high and fairly steady. Everything else being equal, the sustained response results in higher flux levels.

SC4. Effectiveness of main response, P_1 : Its amplitude is heightened during solar minimum and the next two years while its size in (τ, L) and duration increase during those times. The linear coupling is stronger by 6% during solar minimum and by 27% in 1997–1998 compared to

solar maximum. This means that for a given solar wind speed sequence this coupling is more effective during solar minimum than on average. The effectiveness is also quantified with the correlation (6) as discussed below.

SC5. Quasi-adiabatic response: At solar minimum the P_0 peak becomes detached from the rest of the response so that it creates a short-lived isolated radiation belt. Its amplitude decreases which means that for a given solar wind speed sequence it is less effective than on average. Thus the solar wind structures during solar minimum (predominantly high-speed streams) do not excite the quasi-adiabatic mode.

SC6. Narrower range of response during minimum and maximum: The outer boundary of the response is closer to Earth by $\Delta L = -0.4$ at solar minimum and maximum than at intermediate epochs. This indicates that the solar wind activity characteristic of these two epochs does not produce strong effects on the outer part of the radiation belts.

SC7. The model-data correlation is a bimodal function of L shell: The effectiveness of the linear approximation is measured with the correlation (6) and shows a systematic variation with the phase of the solar cycle (Figure 5c). During solar minimum the correlation is high and

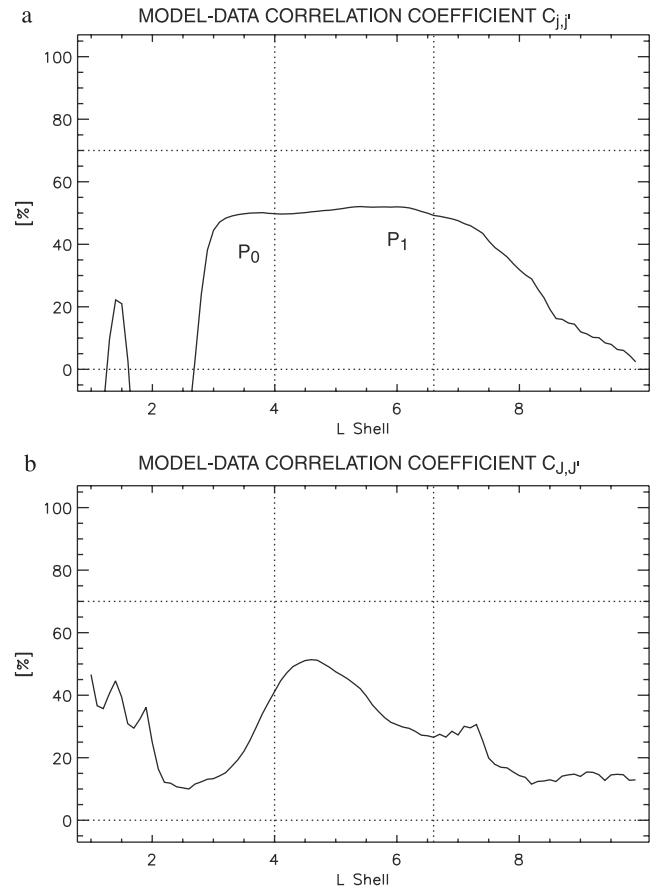


Figure 4. (a) The accuracy of the filter (4) is measured by the correlation (6) between the filter output $j'(t)$ and the observed flux levels $j(t)$. The correlation is a function of L shell. The two broad maxima correspond to peaks P_0 and P_1 . (b) Same as in Figure 4a, but for the fluxes J rather than the log-fluxes j .

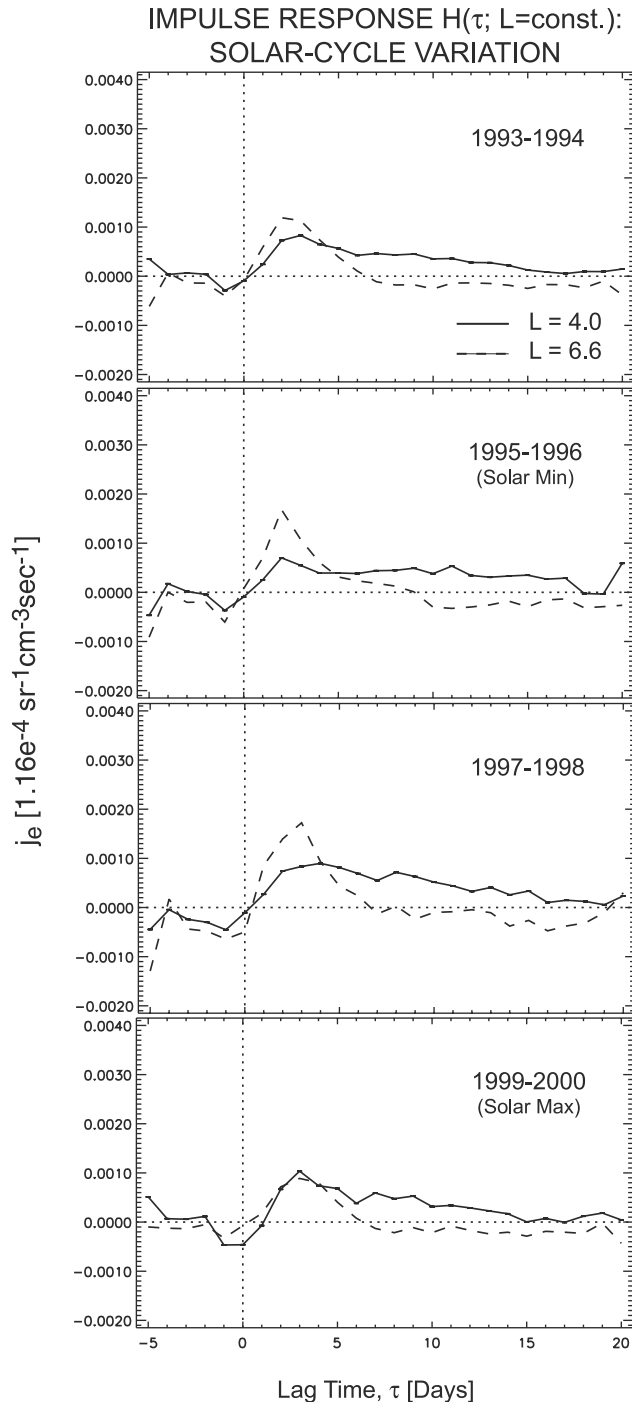


Figure 5a. Variation with solar cycle phase for the filter responses H_4 and $H_{6.6}$. Note the increase in amplitude of both, in particular the response at the geosynchronous region, during or after solar minimum. A similar increase is observed in the duration at those times, especially that of H_4 .

approximately symmetric in L , centered around $L = 5.3$. This peak corresponds to P_1 in the responses of Figure 5b. As we go away from solar minimum, however, a second peak, at least as high, appears at low L shells ($L = 3$ in 1993–1994; 3.6 in 1999–2000). The second peak in correlation corresponds to the P_0 peaks in Figure 5b.

[32] In summary, solar wind conditions in different solar cycle phases reveal different aspects of the electron

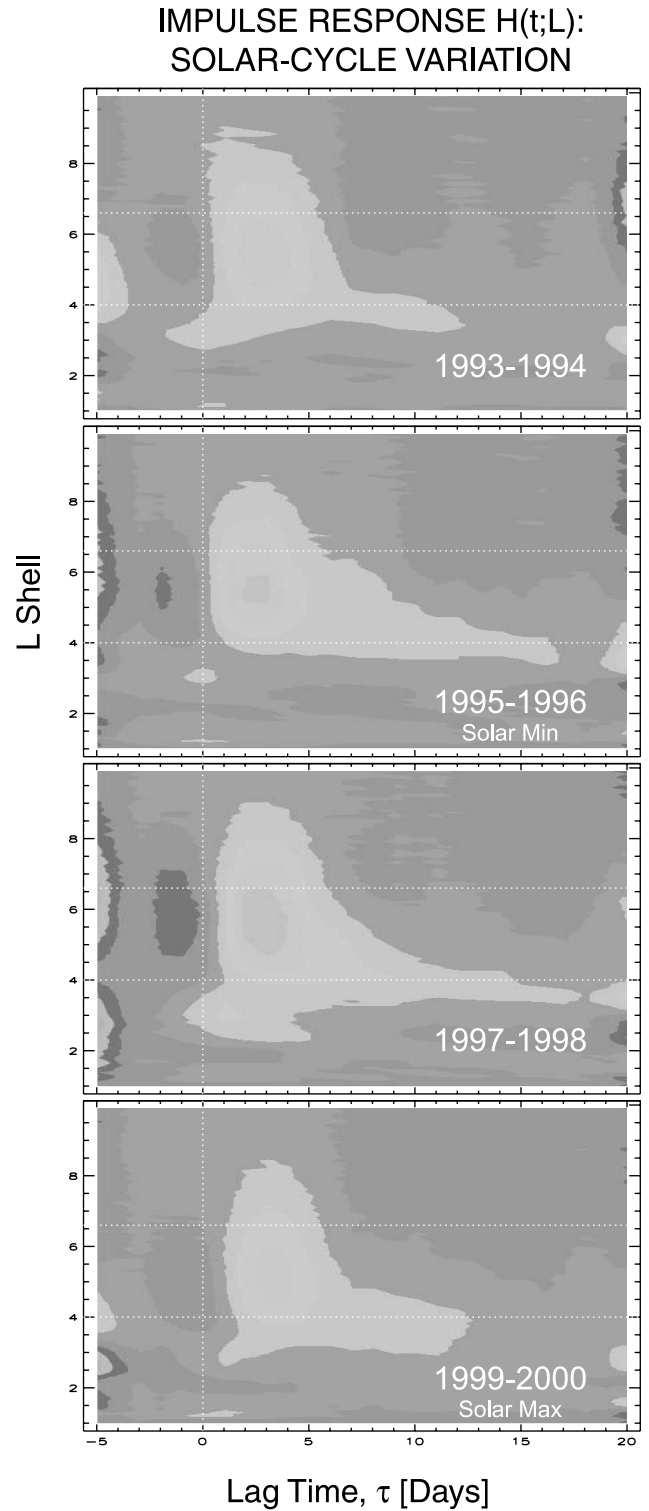


Figure 5b. Same as Figure 5a for response functions at all L shells. Color contours correspond to the scale of Figure 2b. Note the changes in response duration, radial size, amplitude of the main peak P_1 at $(\tau, L) \sim (2, 5)$; and presence and amplitude of the quasi-adiabatic response P_0 at $\sim (0, 3)$. Note that during solar minimum the response becomes more “streamlined” (elliptical) in shape.

MODEL-DATA CORRELATION COEFFICIENT: SOLAR-CYCLE VARIATION

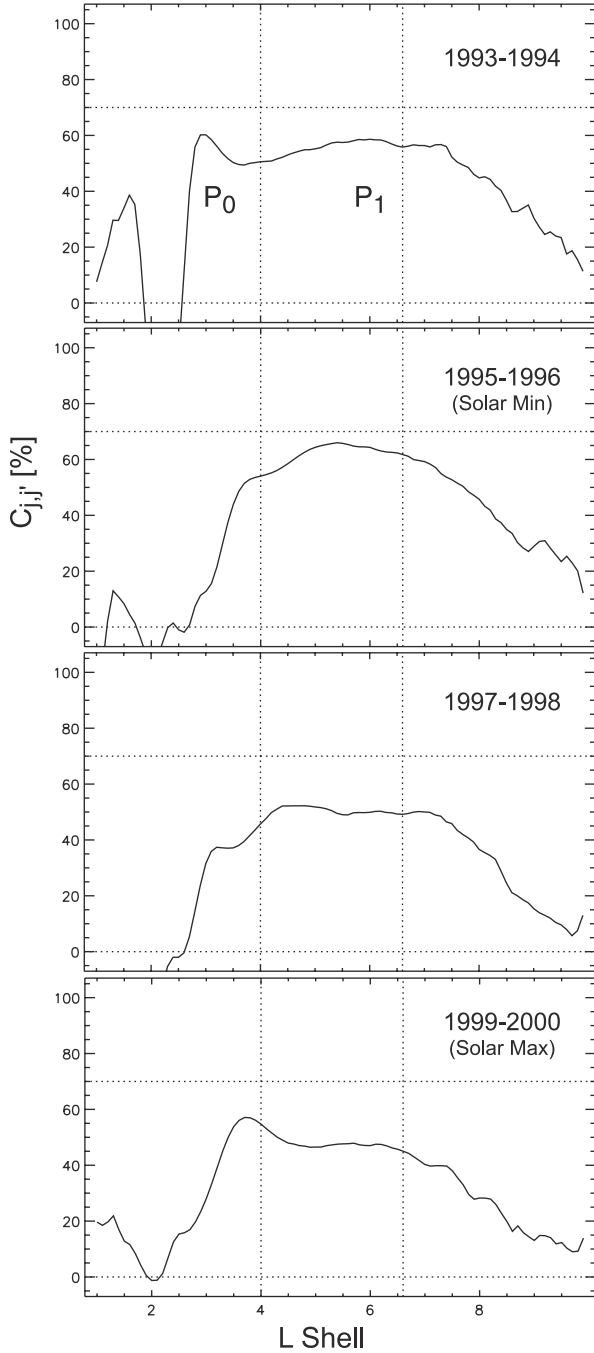


Figure 5c. The correlation function (6) between filter output and observations is shown as a function of L shell. Note that the peak at $L \sim 3$ corresponds to response P_0 as seen in Figure 5b.

response. The high-speed, low-density streams during solar minimum produce a response of higher duration without the quasi-adiabatic peak P_0 . These features produce a fairly “streamlined” appearance in the response in the (τ, L) plane. The radial extent is smaller in solar minimum. On the other hand, during solar maximum higher density inputs

result in higher pressure, which is effective in increasing the electron fluxes at the P_0 peak and over a wider radial extent.

7. Seasonal Variation

7.1. Introduction

[33] Observations over the last decade reveal a systematic variation of electron fluxes as a function of season. They thus provide an insight in the nature and the degree of effectiveness of this particular aspect of solar wind-magnetosphere coupling. The seasonal variation has been measured directly in energetic electron flux levels with equinoctial fluxes being on the average almost three times as high as solstitial ones [Baker *et al.*, 1999, Figure 4]. The finding suggests that the solar wind coupling is more effective in equinoxes than in solstices.

[34] A similar seasonal as well as a diurnal variation in the case of the geomagnetic disturbance level has been discussed and accounted for [Russell and McPherron, 1973, and references therein; Boller and Stolov, 1970; Cliver *et al.*, 2000]. The geomagnetic variation should be distinguished, at least for now, from the electron flux variation since it is known that they are for the most part determined by very different physics, i.e., magnetic reconnection and (probably) viscous interaction.

[35] The seasonal modulation comes about from changes in the activity of the sun and the solar wind (input) as well as changes in the terrestrial environment (response). These effects are not always easily separable:

1. The radial solar wind speed increases with heliographic latitude as a consequence of higher preponderance of coronal holes that emit the fast solar wind. As the ecliptic plane is tilted with respect to the solar equator, Earth is subjected to a seasonally varying solar wind speed (and pressure) profile, as originally put forth in the axial hypothesis [Cortie, 1912]. This effect may be relevant to the electron flux variation because the effective interaction between the solar wind and the inner magnetosphere probably involves a hydrodynamic coupling -since the effect of V_{SW} is more pronounced than any other interplanetary parameter. The coupling may be understood in terms of fluid instabilities (such as Kelvin-Helmholtz) at the magnetopause boundary, mainly at low latitudes. Kinetic effects may further modify the growth rate of the instabilities. Instabilities at the boundary excite ULF waves that transport the kinetic energy in the volume of the inner magnetosphere [Farrugia *et al.*, 2001]. In addition to these variations, periodicities in solar activity [e.g., Bai and Sturrock, 1993] can impose a quasi-regular driving on the inner magnetospheric processes.

2. Earth’s response also depends on season. Assuming for simplicity that the dipole axis is aligned with the rotation axis (this simplification will be removed in point 4 below), the GSM X axis lies closer to the ecliptic plane during equinoxes and is tilted away from it during solstices as shown schematically in Figure 6. (We neglect the magnetotail tilting and warping for distances $>30 R_E$, as irrelevant to the couplings discussed here.)

The modulation of the orientation of the magnetospheric axis produces a time-variable hydrodynamic coupling to the solar wind: The shape and orientation of the effective obstacle that the magnetosphere presents to the oncoming

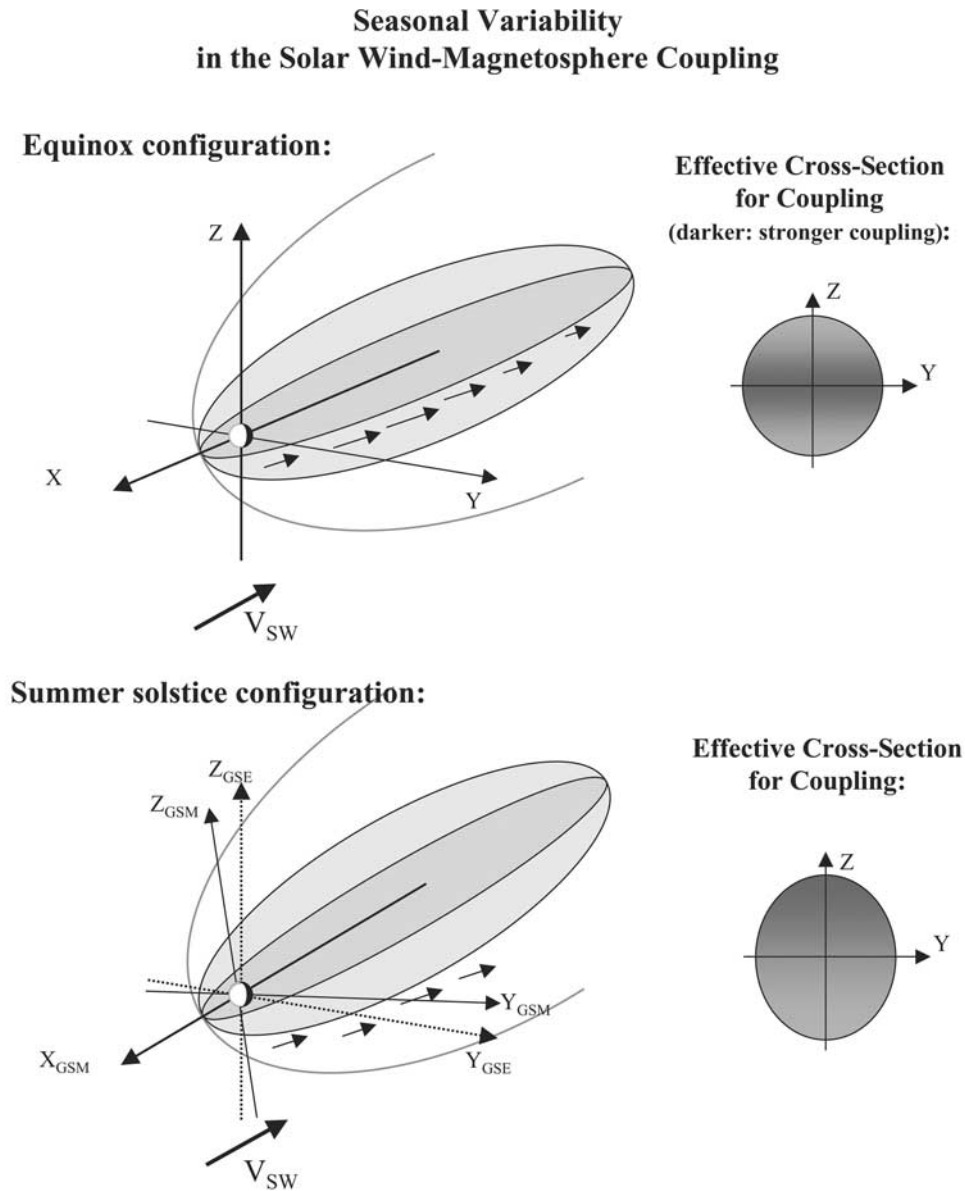


Figure 6. Schematic for the orientation of the magnetosphere during equinox and (summer) solstice. The dipole tilts sunward during the solstice period. The GSE (GSM) axes denote the geocentric solar ecliptic (solar magnetospheric) coordinate system. The small arrows on the dusk flank of the magnetosphere indicate the momentum transferred due to a viscous, hydrodynamic coupling while the shaded ellipse indicates the effective cross-section of the magnetosphere considered as an obstacle placed obliquely in the solar wind flow.

solar wind determine the mechanical and electrodynamic stresses and therefore the energy transfer. So the effective cross-section varies as a function of season, with a larger inclination at solstices presenting a smaller, more asymmetric effective surface for the wind momentum to couple to. The ellipses on the right of the figure show schematically the cross section of the magnetosphere and their shading represents qualitatively the intensity of a simple hydrodynamic momentum transfer [cf. *Farrugia et al.*, 2001].

Several of the above considerations form the basis of the equinoctial hypothesis [Boller and Stolov, 1970], which parameterizes the geomagnetic variation by the angle between solar wind flow and the dipole axis.

Recently the geomagnetic periodicity has been attributed to a lower coupling efficiency during solstices [*Cliver et al.*, 2000] attributed to the equinoctial hypothesis. The seasonal modulation of the electron flux is probably another effect of this variation in coupling efficiency.

3. From a magnetic reconnection perspective the most important interplanetary input variable is the amplitude of the geomagnetic component antiparallel to Earth's dipole axis (or GSM z axis). Additionally the GSE y component can contribute to or reduce the GSM z component and thereby the reconnection efficiency, and production of seed electrons. The B_y effect is the main part of the Russell-McPherron effect [Russell and McPherron, 1973]. It is

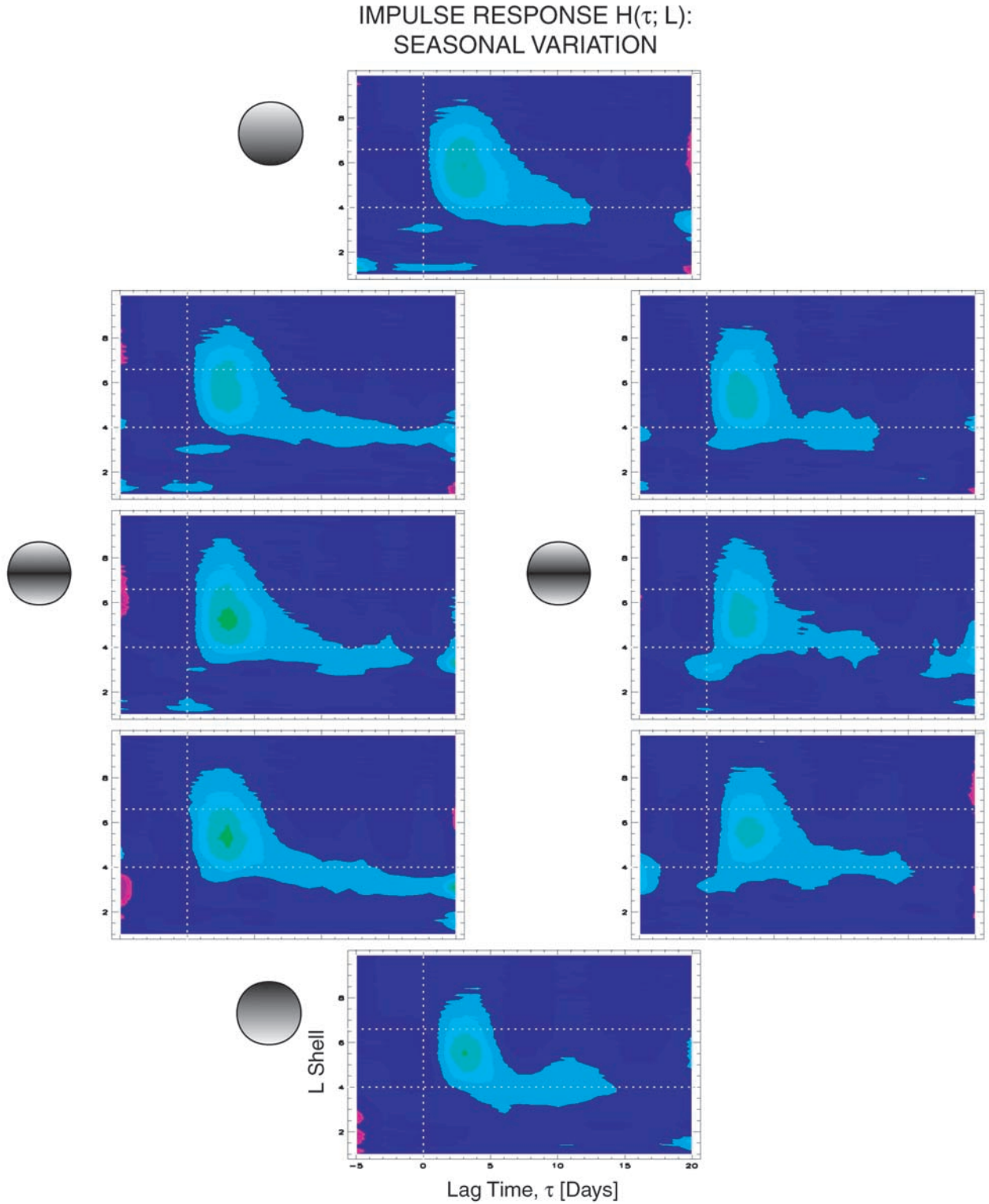


Figure 7a. Seasonal variation of the response function (4). The shaded ellipses introduced in Figure 6 indicate schematically the intensity and latitudinal asymmetry of the coupling.

clearly important in the geomagnetic variation, but is also involved in the electron flux variation.

Under certain conditions the Russell-McPherron effect has a seasonal periodicity. The time-averaged solar wind

magnetic field is organized in long-lived spatial structures, the sectors, related to slowly varying structures on the solar surface. These are characterized by specific sign of the B_y component, as “outward” (B_y positive in the GSE

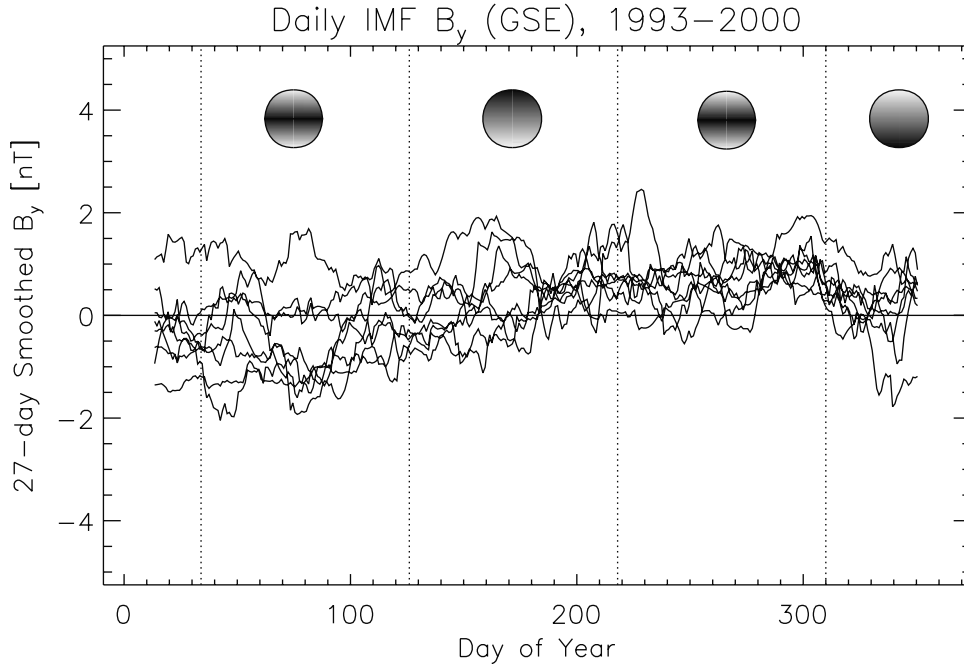


Figure 7b. Annual profiles of the IMF B_y component (GSE coordinate system) during the 8 years of SAMPEX measurements. The year is divided in ~ 92 -day intervals, which are marked with the shaded ellipses of Figure 6. Note the smaller average B_y during spring contrasted to the positive component during fall equinox.

coordinate system) or “inward” (B_y negative). As the solar wind structures rotate past the Earth the GSE B_y component displays a clear periodicity in a given year. Because the periods of the solar rotation and Earth’s revolution around the Sun are nearly commensurate, the periodicity occurs at approximately the same time each year for several successive years. Thus in a data set which spans less than one solar cycle the B_y effect can appear as a “seasonal” variation.

4. The dipole axis does not coincide with the rotation axis, as assumed in point 2 for simplicity, but it is inclined relative to it by about 11.5° . This produces diurnal variations in both the Russell-McPherron and Boller-Stolov effects (and any other coupling that depends on magnetic reconnection), which are different and can be used to distinguish among them [Cliver *et al.*, 2000].

[36] From these (points 1–4) and many other considerations it is evident that the seasonal variation is determined by both large-scale energy transfer mechanisms (reconnection as well as viscous interaction) and many other minor effects. These are important in understanding the analysis of the SAMPEX measurements.

7.2. Modeling and Results

[37] We measure the variation in the coupling as a function of season in terms of amplitude, radial extent, and duration of the response $H(\tau; L)$. We have separated each year’s data in 92-day intervals centered at equinoxes, solstices, and intermediate points. We have combined the data from all 8 years for each such interval. A daily flux measurement is associated, as before, with a window of V_{SW} data of $T_s = -5$ preceding days and $T = 21$ following ones. Note that only every other one out of the 8 intervals so defined are independent measurements

(e.g. intervals 1, 3, 5, and 7): the intermediate intervals contain half of each of their neighbor’s interval (46 days) and do not provide new information. They are included to facilitate visualization.

[38] The impulse responses $H(\tau; L)$ are shown in Figure 7a. The winter and summer solstices are at the top and bottom, respectively, while the filters for the other six intervals are arranged in a clockwise fashion. The shaded ellipses indicate qualitatively the cross-section, efficiency, and degree of North-South asymmetry of the coupling. We note several effects and asymmetries in the seasonal response (SE) and discuss them in the next section:

SE1. Equinox-solstice asymmetry in radial size of the responding region: The radial extent ΔL of $H(\tau; L)$ of the main response, P_1 , is larger for equinoxes

$$\Delta L_{F,Sp} > \Delta L_{W,Su},$$

i.e., the linearly responding region is more extended. A second, qualitative difference is that the shape of the (τ, L) region is more elliptic in the solstices and linear in the equinoxes, so during solstices the coupling is initiated later and is lower as we go away from the central region of $L = 4.5 - 6$. The weaker linear coupling may be related to the reduced production of high-energy electrons during solstices.

SE2. Weaker quasi-adiabatic response during solstices: At those times the P_0 peak at $(\tau, L) = (0, 3)$ is either weaker (winter) or missing altogether (summer). In equinoxes, in contrast, the peak is comparable to P_1 and the overall response profile in $(\tau; L)$ is similar to the long-term-average response in Figure 2b:

$$H_{F,Sp}^{(P_0)} \gg H_{W,Su}^{(P_0)} \approx 0.$$

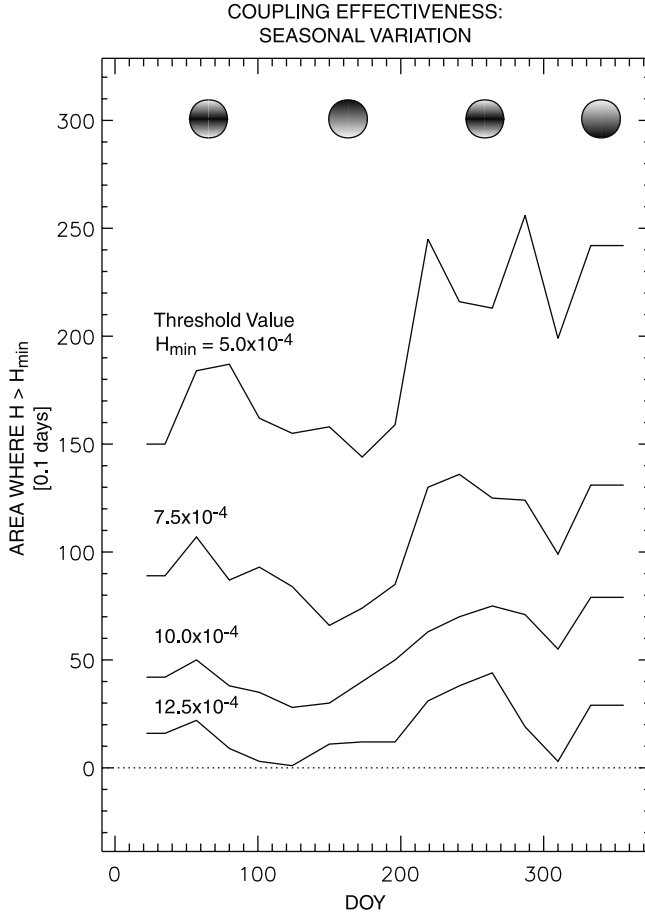


Figure 7c. Average annual profile of the area (8) measuring the effectiveness of the coupling. Seasons are indicated by the shaded ellipses at the top. For low H_{\min} the minima at the solstices indicate weak coupling. As the area H_{\min} is increased an additional fall-spring asymmetry appears, perhaps due to the increased B_y during fall (Figure 7b). This shows the semiannual variation of peak P_1 and the annual variation of the wider region around P_0 and P_1 .

As discussed in the last two sections, this peak is a quasi-adiabatic response to solar wind pressure increases. Therefore during solstices the orientation of the magnetosphere (and perhaps also its heliographic latitude) is such that solar wind compressions are not as effective. This is in agreement with the results of *Baker et al.* [1999]. In addition, the radial velocity is lower during solstices rather than equinoxes.

SE3. Fall-spring asymmetry in the response duration: The duration T of the main coupling in the P_1 region is much longer for fall

$$T_F \gg T_{Sp}$$

by at least 2 days and up to 10, depending on the H contour chosen for the comparison. A similar fall-spring asymmetry is evident in the fluxes as well as shown by *Baker et al.* [1999, Figure 4], although it is much weaker (about 3%).

One possible reason for this asymmetry may be the average orientation of the IMF B_y component according to the *Russell and McPherron* [1973] effect. In the years

1993–2000 the average B_y in GSE is smaller and negative in spring followed by a stronger, positive field in fall (Figure 7b). The average and standard deviation of the B_y component is

$$\begin{aligned} \langle B_y^{(GSE)} \rangle_{Sp} &= -0.27 \pm 0.74 \text{ nT} \\ \langle B_y^{(GSE)} \rangle_F &= 0.66 \pm 0.45 \text{ nT} \end{aligned}$$

In spring this negative $B_y^{(GSE)}$ component is projected on the Northward part of $B_z^{(GSM)}$ thus not contributing to antiparallel reconnection, while in fall the positive $B_y^{(GSE)}$ projects on the Southward part thereby increasing the field available for antiparallel reconnection. Another reason may be a seasonal modulation of the velocity (X. Li, private communication, 2001).

SE4. Fall-winter versus spring-summer asymmetry in coupling effectiveness: The coupling is stronger later in the year than in the first two seasons. To quantify this effect we define a strong coupling region in (τ, L) as the region where the response exceeds a given amplitude, $H > H_{\min}$. Its spatiotemporal area is

$$A_{\text{eff}} = \int_{H > H_{\min}} d\tau dL. \quad (8)$$

The area (8) is lowest during summer and winter showing that the coupling is weaker during those times. For high values of H_{\min} (e.g. $5.0 \times 10^{-4} \text{ day}^{-1}$) the minima are close to the solstice times, and therefore A_{eff} has an annual variation.

Decreasing the threshold value H_{\min} leads to an increase in the area A_{eff} of the enclosed region. More important, however, is a change in the annual variation: the summer minimum drifts to later times in the year. Second, the periodicity changes from semiannual to annual: the fall-spring symmetry noted above is evident in Figure 7c. The area A_{eff} is larger by approximately 50% for the fall and winter responses than for the other two intervals. This effect is the same for several choices of the threshold value, H_{\min} , as shown in the figure.

Note that for large values of H_{\min} the region A includes only the area around P_1 , but as H_{\min} is lowered it eventually includes both peaks P_0 and P_1 . Thus each mode of response has a different periodicity, summarized as follows

$$\begin{aligned} P_0 &: \text{Annual variation} \\ P_1 &: \text{Semiannual variation} \end{aligned} \quad (9)$$

This difference is a strong indicator of different physical processes.

SE5. Fall and winter versus spring and summer asymmetry in the model-data correlation: The correlation (6) varies with season in a way similar to the periodicities (9). The correlation is shown as a function of L shell in Figure 7d. The panels are arranged in clockwise order, similar to the filter responses in Figure 7b. The correlation at low L , corresponding to the P_0 peak, is significant during spring and summer (marked with a vertical arrow). As a result the correlation function $C(L)$ is bimodal in spring in spring and summer and unimodal in fall and

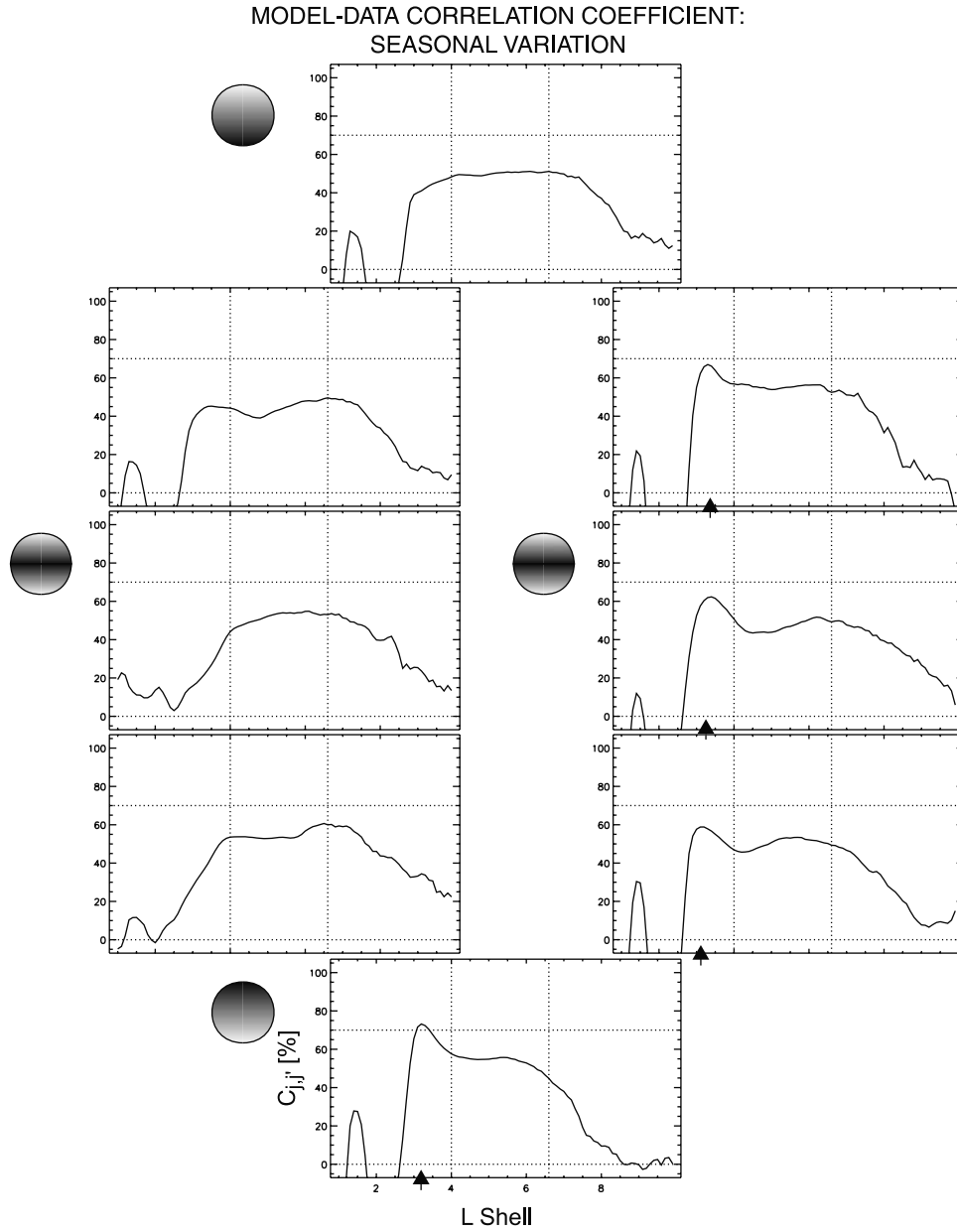


Figure 7d. Similar seasonal variation as in Figure 7a for the correlation (6) of the model-data fit.

winter. The correlation in a L range around this peak varies as follows:

$$\begin{aligned} C^{(Sp,Su)}(3 \leq L \leq 3.5) &= 60 - 70\% \\ C^{(F,W)}(3 \leq L \leq 3.5) &= 25 - 40\% \end{aligned}$$

Thus the correlation around P_0 has an annual periodicity, similar to the P_0 variation (9) of the area. Therefore the effect of the quasi-adiabatic response has an annual periodicity.

8. Summary and Discussion

[39] We have examined the temporal and spatial variability of dynamic response in the inner magnetosphere electron environment. We have used a first-order (linear)

approximation to a very complex set of nonlinear phenomena and discussed the advantages and limitations of the approach. We have also quantified the accuracy of this method in reproducing the data.

[40] The linear analysis has shown two main temporal and spatial regions in the response. The main response, P_1 , is in the range $L = 4 - 6.6$ centered at 5.3 with fluxes j rising simultaneously over a wide area of $\Delta L > 5$ in 2–3 days after an increase in the solar wind. Fluxes at greater altitudes rise at the same time, but then decay much more rapidly. The overall duration of the response scales with L as:

$$T - \tau_{P_1} \sim \begin{cases} a_1 L, & \tau_{P_1} \leq \tau \leq \tau_b \\ a_2 L, & \tau_b \leq \tau \end{cases}, \quad (10)$$

where $\tau_{P_1} = 2$ days, $\tau_b = 7.5$ days, and $a_1/a_2 \sim 6-10$, (we have neglected the $b_{1,2}$ coefficients). The coefficients in (10) are approximate (see Table 1).

[41] A quasi-adiabatic response, P_0 , occurs in the region $(\tau, L) \sim (0, 3)$, i.e. at the time of solar wind impact. It probably represents events of rapid acceleration of electrons deep in the magnetosphere following extremely high compressions by shocks or CMEs [e.g., *Li et al.*, 1993; *Baker et al.*, 1998]. This transient response is a prominent characteristic of the linear response during solar maximum. We have called this a “quasi-adiabatic” response because of its timing at zero lag and its short duration. However, there is an ambiguity in that term because of (1) limitations in the magnetic field model, and (2) the lack of pitch angle information from the SAMPEX/PET instrument that would have enabled the calculation of the phase space density. On the other hand, the linear filter procedure we use averages over many different solar wind conditions and can thereby significantly reduce the adiabatic part of the response.

[42] The effect of different types of solar wind structure is investigated by examining the response over a large part of a solar cycle. Statistically the highest response occurs during solar minimum, probably due to the sustained solar wind speed of streams. The density of high-speed streams is low and this is probably the reason why there is no significant quasi-adiabatic response P_0 .

[43] Whereas the solar cycle dependence shows the response to different levels of disturbance, the seasonal dependence gives information about the location of the magnetosphere relative to the equatorial current sheet and its inclination relative to the solar wind flow direction.

1. Peak P_0 is a response to initial, short-lived density increases that are stronger during equinoxes. At those times Earth crosses the heliospheric equatorial plane and its GSM X axis is approximately parallel to that plane. This appears to be a hydrodynamic effect that does not involve the magnetic field and therefore consistent with the equinoctial hypothesis.

2. The radial size of the responding region varies with season as well. It increases for equinoxes compared to solstices. The radial size of the responding regions is larger, the closer the dipole axis is to the normal to the ecliptic. In that case the GSM x-axis lies on the ecliptic plane. A longer radial extent provides a larger region for hydrodynamic coupling. At solstices this effect is reverse, because the radial extent is smaller leading to a less effective coupling. This is also inferred from the geomagnetic variation [*Cliver et al.*, 2000].

3. A different type of asymmetry occurs between fall and spring equinoxes. The response lasts several days longer in fall.

[44] In general, seasonal variations are not explained by either the axial or the equinoctial hypothesis alone, but are probably a combination of both effects as well as the Russell-McPherron effect. In summary, linear filter models accounts for a part of the effect of solar wind speed on the electron fluxes of the inner magnetosphere and give new insights into the long-term and regular variability. Non-linear effects of the interaction, and effects of radial transport and local acceleration, will necessitate more complex models.

[45] **Acknowledgments.** We thank D. Berdichevsky, R. Friedel, S. Ghosh, X. Li, M. Temerin, and V. Uritsky for discussions. IMF data were obtained from the OMNI database of NASA's NSSDC. D. V. was supported by NSF GEM and NASA SR&T grants.

[46] Janet G. Luhmann thanks Michael Temerin and Tsogunobu Nagai for their assistance in evaluating this paper.

References

- Abel, B., and R. M. Thorne, Electron scattering loss in Earth's inner magnetosphere, 1, Dominant physical processes, *J. Geophys. Res.*, **103**, 2385, 1998.
- Bai, T., and P. A. Sturrock, Evidence for a fundamental period of the Sun and its relation to the 154-day complex of periodicities, part 1, *Astrophys. J.*, **409**(1), 476–486, 1993.
- Baker, D. N., J. B. Blake, L. B. Callis, R. D. Belian, and T. E. Cayton, Relativistic electrons near geostationary orbit: Evidence for internal magnetospheric acceleration, *Geophys. Res. Lett.*, **16**, 559–562, 1989.
- Baker, D. N., R. L. McPherron, T. E. Cayton, and R. W. Klebesadel, Linear prediction filter analysis of relativistic electron properties at 6.6 RE, *J. Geophys. Res.*, **95**, 15,133–15,140, 1990.
- Baker, D. N., et al., A strong CME-related magnetic cloud interaction with the Earth's magnetosphere: ISTP observations of rapid relativistic electron acceleration on May 15, 1997, *Geophys. Res. Lett.*, **25**, 2975–2978, 1998.
- Baker, D. N., S. G. Kanekal, T. I. Pulkkinen, and J. B. Blake, Equinoctial and solstitial averages of magnetospheric relativistic electrons: A strong semiannual modulation, *Geophys. Res. Lett.*, **26**, 3193–3196, 1999.
- Boller, B. R., and H. L. Stolov, Kelvin-Helmholtz instability and the semi-annual variation of geomagnetic activity, *J. Geophys. Res.*, **75**, 6073–6084, 1970.
- Clauer, C. R., The technique of linear prediction filters applied to studies of solar wind-magnetosphere coupling, in *Solar Wind-Magnetosphere Coupling*, edited by Y. Kamide and J. A. Slavin, pp. 39–57, Terra Sci., Tokyo, 1986.
- Cliver, E. W., Y. Kamide, and A. G. Ling, Mountains versus valleys: Semiannual variation of geomagnetic activity, *J. Geophys. Res.*, **105**, 2413–2424, 2000.
- Cook, W. R., et al., PET: A Proton Electron Telescope for studies of magnetospheric, solar, and galactic particles, *IEEE Trans. Geosci. Remote Sens.*, **31**(3), 565–571, 1993.
- Cortie, A. L., Sunspots and terrestrial magnetic phenomena, 1898–1911: The cause of the annual variation in magnetic disturbances, *Mon. Not. R. Astron. Soc.*, **73**, 52, 1912.
- Crooker, N. U., Solar and heliospheric geoeffective disturbances, *J. Atmos. Sol. Terr. Phys.*, **62**(12), 1071–1085, 2000.
- Elkington, S. R., M. K. Hudson, and A. A. Chan, Acceleration of relativistic electrons via drift-resonant interaction with toroidal-mode Pc5 ULF oscillations, *Geophys. Res. Lett.*, **26**, 3273–3276, 1999.
- Farrugia, C. J., F. T. Gratton, and R. B. Torbert, Viscous-type processes in the solar wind-magnetosphere interaction, *Space Sci. Rev.*, **95**(1–2), 443–456, 2001.
- Kanekal, S. G., D. N. Baker, J. B. Blake, B. Klecker, R. A. Mewaldt, and G. M. Mason, Magnetospheric response to magnetic cloud (coronal mass ejection) events: Relativistic electron observations from SAMPEX and Polar, *J. Geophys. Res.*, **104**, 24,885–24,894, 1999.
- Koons, H. C., and D. J. Gorney, A neural network model of the relativistic electron flux at geosynchronous orbit, *J. Geophys. Res.*, **96**, 5549–5556, 1991.
- Koons, H. C., J. B. Blake, and J. Mazur, The impact of the space environment on space systems, *TR-99 (1670)-1*, Aerospace Corp., El Segundo, Calif., 1999.
- Li, X., and M. A. Temerin, The electron radiation belt, *Space Sci. Rev.*, **95**(1–2), 569–580, 2001.
- Li, X., I. Roth, M. Temerin, J. R. Wygant, M. K. Hudson, and J. B. Blake, Simulation of the prompt energization and transport of radiation belt particles during the Marth 24, 1991 SSC, *Geophys. Res. Lett.*, **20**, 2423–2426, 1993.
- Li, X., D. N. Baker, M. A. Temerin, D. Larson, R. P. Lin, E. G. D. Reeves, M. D. Looper, S. G. Kanekal, and R. A. Mewaldt, Are energetic electrons the source of the outer radiation belts?, *Geophys. Res. Lett.*, **24**, 923–926, 1997.
- Li, X., M. Temerin, D. N. Baker, G. D. Reeves, and D. Larson, Quantitative prediction of radiation belt electrons at geostationary orbit based on solar wind measurements, *Geophys. Res. Lett.*, **28**, 1887–1890, 2001.
- Liu, W. W., G. Rostoker, and D. N. Baker, Internal acceleration of relativistic electrons by large-amplitude ULF pulsations, *J. Geophys. Res.*, **104**, 17,391–17,407, 1999.
- Nagai, T., Space weather forecast: Prediction of relativistic electron intensity at synchronous orbit, *Geophys. Res. Lett.*, **15**, 425–428, 1988.

- Paulikas, G. A., and J. B. Blake, Effects of the solar wind on magnetospheric dynamics: Energetic electrons at the synchronous orbit, in *Quantitative Modeling of Magnetospheric Processes*, *Geophys. Monogr. Ser.*, vol. 21, pp. 180–200, AGU, Washington, D. C., 1979.
- Press, W. H., B. P. Flannery, S. A. Teukolsky, and W. V. Vetterling, *Numerical Recipes: The Art of Scientific Computing*, Cambridge Univ. Press, New York, 1993.
- Rostoker, G., S. Skone, and D. N. Baker, On the origin of relativistic electrons in the magnetosphere, *Geophys. Res. Lett.*, 25, 3701–3704, 1998.
- Russell, C. T., and R. L. McPherron, Semiannual variation of geomagnetic activity, *J. Geophys. Res.*, 78, 92–107, 1973.
- Selesnick, R. S., and J. B. Blake, On the source location of the radiation belt relativistic electrons, *J. Geophys. Res.*, 105, 2607–2624, 2000.
- Selesnick, R. S., J. B. Blake, W. A. Kolasinski, and T. A. Fritz, A quiescent state of 3 to 8 MeV radiation belt electrons, *Geophys. Res. Lett.*, 24, 1343–1346, 1997.
- Tsutai, A., C. Mitsui, and T. Nagai, Predictions of a geosynchronous electron environment with in situ magnetic field measurements, *Earth Planets Space*, 51(3), 219–233, 1999.
- Volkmer, P. M., and F. M. Neubauer, Statistical properties of fast magnetoacoustic shock waves in the solar wind between 0.3 and 1 AU – Helios 1, 2 observations, *Ann. Geophys.*, 3(1), 1–12, 1985.

D. N. Baker and S. G. Kanekal, Laboratory for Atmospheric and Space Physics, University of Colorado, Boulder, CO 80309, USA.

A. J. Klimas, NASA Goddard Space Flight Center, Greenbelt, MD 20771, USA.

D. Vassiliadis, Universities Space Research Association, NASA Goddard Space Flight Center, Code 690.2, Greenbelt, MD 20771, USA. (vassi@electra.gsfc.nasa.gov)

R. S. Weigel, National Research Council, NASA Goddard Space Flight Center, Greenbelt, MD 20771, USA.